

Ultrahigh-Working-Frequency Embedded Supercapacitors with 1T Phase MoSe₂ Nanosheets for System-in-Package Application

Zhi Jiang, Yang Wang, Shuoguo Yuan, Lu Shi, Ni Wang, Jie Xiong, Wenhui Lai, Xuanyu Wang, Feiyu Kang, Wei Lin, Ching Ping Wong, and Cheng Yang*

Commercial aluminium electrolyte capacitors (AECs) are too large for integration in future highly integrated electronic systems. Supercapacitors, in comparison, possess a much higher capacitance per unit volume and can be embedded as passive capacitors to address such challenges in electronics scaling. However, the slow frequency response ($<10^1$ Hz) typical of supercapacitors is a major hurdle to their practical application. Here, it is demonstrated that 1T-phase MoSe₂ nanosheets obtained by laser-induced phase transformation can be used as an electrode material in embedded micro-supercapacitors. The metallic nature of MoSe₂ nanosheet-based electrodes provides excellent electron- and ion-transport properties, which leads to an unprecedented high-frequency response (up to 10^4 Hz) and cycle stability (up to 10^6 cycles) when integrated in supercapacitors, and their power density can be ten times higher than that of commercial AECs. Furthermore, fabrication processes of the present device are fully compatible with system-in-package device manufacturing to meet stringent specifications for the size of embedded components. The present research represents a critical step forward in in-package and on-chip applications of electrolytic capacitors.

1. Introduction

Future electronic systems will feature even higher integration level, with isolated components and modules in a single package (system-in-package, SiP) or even on a chip (system-on-chip, SoC). These systems require all components to have better performance and smaller size to cater to the burgeoning wearable electronics and internet of things (IOTs) markets.^[1] In order to obtain a shorter interconnection distance and more compact size, isolated components (e.g., resistors and capacitors) with miniature size embedded into substrates is urgently needed.^[2] Aluminium electrolyte capacitors (AECs) represent a typical example, which occupy $\approx 1/3$ of the global capacitor market with an annual shipment of ≈ 170 billion pieces.^[3] Currently, the smallest commercial AECs are still around dozens of cubic millimetres in size, their thickness is much thicker than

common circuit substrates, and their size is generally larger than all available passive components. Considering the fact that current commercial embedded components usually have a largest dimension of <1 mm (for embedded dies) or thickness <200 μm (for embedded circuits), developing embeddable electrolytic capacitors with both a high capacitance and small form factor remains an important yet challenging task.

Typical capacitors, including AECs, tantalum capacitors, and ceramic capacitors, store potential energy by collecting charges on the plane electrodes, which is very limited by their surface area. All of them have ceiling working frequencies, depending on their physical working mechanisms, beyond which they can only behave as a resistor. As compared, supercapacitors (SCs) can deliver much higher specific capacitance,^[4] rendering it possible to discharge electricity with more compact component size. However, due to the nature of electrochemical capacitors, most available SCs only work at relatively low frequencies (e.g., 10^0 Hz), largely inhibiting their electronic applications (Figure 1). Recently, researchers have developed SC technologies with novel electrode materials and structures, and some of the breakthroughs have laid important foundations for future embedded SC components, such as transferrable thin-film SCs, tailorable thin-film SCs, and surface-mountable SCs.^[1,5-7] Despite these exciting progresses, novel materials with

Z. Jiang,^[+] Dr. Y. Wang,^[++] S. Yuan,^[++] L. Shi, W. Lai, X. Wang, Prof. F. Kang, W. Lin^[+++], Prof. C. Yang
Division of Energy and Environment
Graduate School at Shenzhen
Tsinghua University
Shenzhen 518055, China
E-mail: yang.cheng@sz.tsinghua.edu.cn

Prof. N. Wang, Prof. J. Xiong
State Key Laboratory of Electronic Thin Films and Integrated Devices
University of Electronic Science and Technology of China
Chengdu 610054, China

Prof. F. Kang
Tsinghua-Berkeley Shenzhen Institute
Tsinghua University
Shenzhen 518055, China

Prof. C. P. Wong
School of Materials Science and Engineering
Georgia Institute of Technology
771 Ferst Dr, Atlanta, GA 30332, USA

^[+]Present address: Department of Electrical Engineering and Information Systems, Graduate School of Engineering, The University of Tokyo, Japan

^[++]Present address: Department of Applied Physics, The Hong Kong Polytechnic University, Hong Kong, China

^[+++]Present address: Apple Inc, 19333 Vallco Pkwy, Cupertino, CA 95014, USA

DOI: 10.1002/adfm.201807116

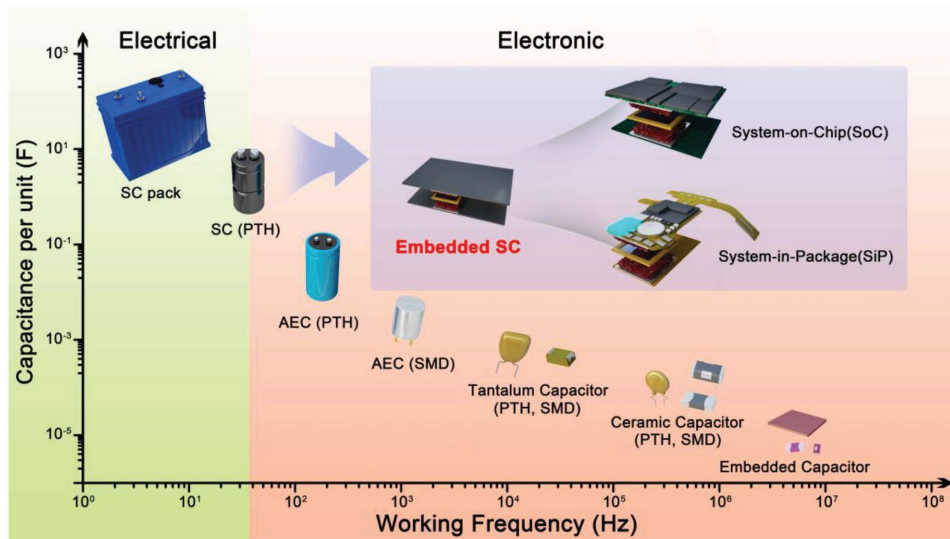


Figure 1. Schematic of different kinds of capacitors with different working principles and packaging techniques. The capacitance per unit decreases with the device size. The SCs, AEC, tantalum capacitor, and ceramic capacitor are listed in the order of working frequency and capacitance per unit. These devices can be in the form of packs, pin-through-hole (PTH) units, SMD units, and embedded units.

improved charge-storage/transfer properties are still urgently needed. Among the available electrode materials, 2D materials, e.g., graphene, transition metal carbides (MXenes), and transition metal chalcogenides (TMDs), have been regarded as the most promising candidates for electrode materials due to their high-rate and capacity performances resulted from their high specific surface areas, excellent electronic conductivity, and well-ordered micro/nanostructures.^[8] Graphene electrodes have been intensively studied, and high-rate capabilities at 10^3 V s^{-1} was achieved.^[8–10] Nevertheless, due to the poor wettability between electrolyte and electrode, it is difficult to further enhance their rate performance because the hydrophobic nature of carbon.^[8–10] Pseudocapacitive MXene-based electrodes that can deliver a capacitance density of over 300 F g^{-1} when working at 10^2 V s^{-1} was recently reported, surpassing the best known carbon-based supercapacitors in terms of capacity.^[11] For even higher working frequencies, electric-double-layer-type SCs would be more competitive than pseudocapacitive SCs due to the much faster discharge rate.

Very recently, TMD nanosheets, such as VS_2 ,^[12] MoS_2 ,^[13] WS_2 ,^[14] and MoSe_2 ,^[15] have shown strong potential as electric-double-layer-type or pseudocapacitive electrode materials for SCs. For example, 2H-phase MoSe_2 nanosheets can achieve a very high specific capacitance (i.e., 1114.3 F g^{-1}) at low charging/discharging rates, but this material showed unsatisfactory frequency response and rate capability due to their relatively low electrical conductance.^[15,16] On the other hand, their metallic-phase counterparts display much higher electrical conductivity, thus showing great promise for electrodes.^[13,17,18] For instance, the natural 2H phase can be converted into the metallic 1T phase via organolithium chemical reaction, which can simultaneously exfoliate bulk MoS_2 powders into monolayer nanosheets with a conversion rate of 70%; this electrode material exhibited a high volumetric capacitance ($400\text{--}700 \text{ F cm}^{-3}$) and good cycle stability over 5000 cycles.^[13] Recently, TMD nanosheets were also produced using the mechanical exfoliation method in ambient

air,^[19] and these nanosheets were converted into the metallic 1T phase by laser irradiation treatment^[16,20]; however, electrochemical energy storage in the laser-induced-transformed 1T TMD has not been reported.

So far, it is still challenging to simultaneously achieve high capacity and high working frequency in small-size SCs for the application in embedded devices. Current commercial AECs in Figure 1 show a relatively high capacitance level and moderate frequency response (as high as $10^3\text{--}10^4 \text{ Hz}$), yet their component size is very large, and their specific energy is relatively low (on the level of $10^{-4} \text{ Wh cm}^{-3}$). Even though SCs show the highest energy density ($\approx 10^{-1} \text{ Wh cm}^{-3}$) in the family of capacitors, their weak capacitance performance at higher working frequencies becomes a major hurdle for wider electronic applications, especially for future on-chip and in-system energy/signal managements, where high working frequencies are necessary. Novel SC components that can be embedded into a high-density-integration system are highly desired, and their working frequency should match or exceed that of AECs, both of which are extremely important yet have not been achieved.

Here, we show that by UV laser irradiation, the naturally occurring 2H phase MoSe_2 nanosheets can almost 100% transform into 1T phase (L- MoSe_2), which can be used to fabricate embedded SC components for SiP and SoC applications (exploded schematics are shown in Figure 1), which exhibit unprecedented rate capability (up to 10^4 Hz with a phase angle $> 60^\circ$ and relaxation time of $\approx 32 \mu\text{s}$) and cycle stability (insignificant capacitance loss after 10^6 cycles). These SCs can deliver a maximal energy density of 62.6 mWh cm^{-3} , which is even higher than that of lithium thin-film batteries, while manifesting a superhigh power density of 2113 W cm^{-3} , which is higher than the reported results of state-of-the-art SCs and is approximately ten times higher than that of commercial AECs. In addition, all involved fabrication processes are fully compatible with the green manufacturing of miniaturized devices to meet stringent specifications for the size of embedded

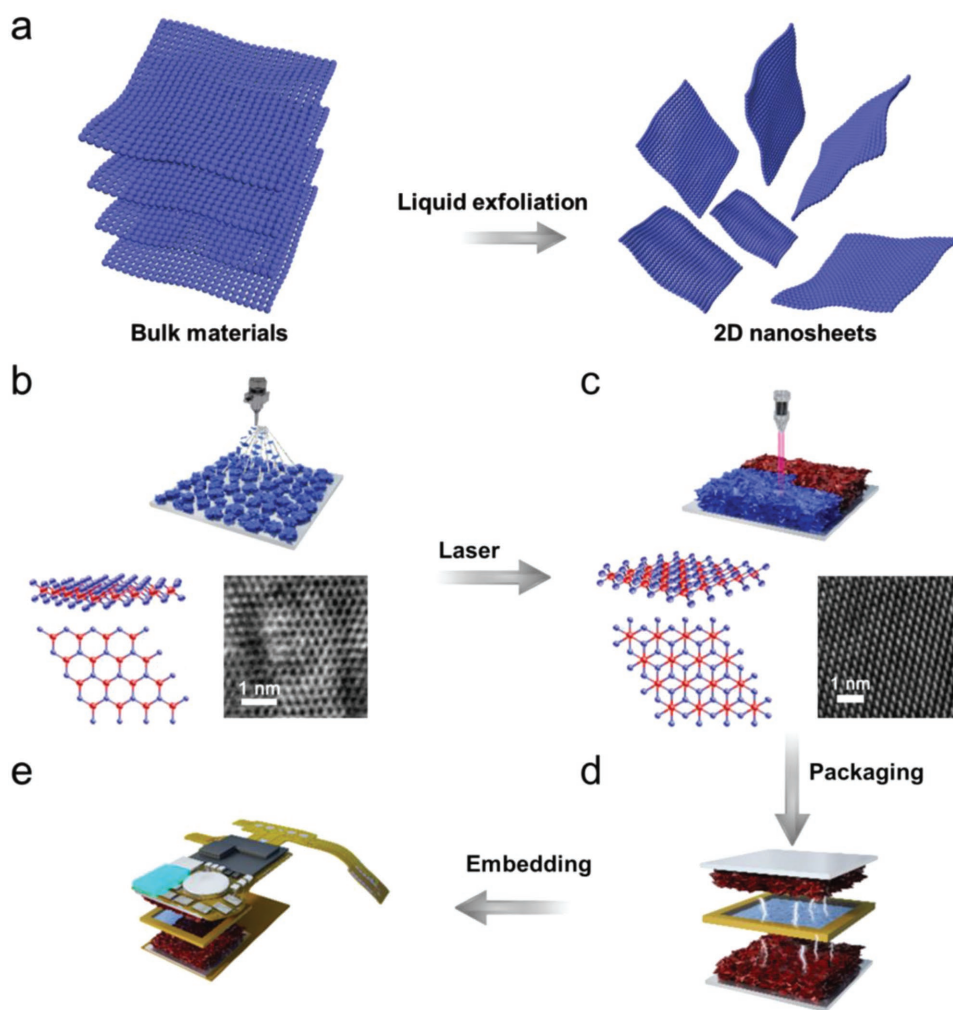


Figure 2. Fabrication route for laser-processed 1T MoSe₂ electrodes and embedded SCs. a) Fabrication of 2D nanosheets from bulk materials by the liquid exfoliation method. b) The 2H MoSe₂ nanosheets are electrospayed onto the current collector. A molecular model of 2H MoSe₂ and high-resolution transmission electron microscopy (HR-TEM) image of the 2H MoSe₂ nanosheets are also shown. c) The 2H MoSe₂ nanosheets are transformed into the 1T phase by laser irradiation treatment. A molecular model of 1T L-MoSe₂ and HR-TEM image of the 1T MoSe₂ nanosheets obtained by laser treatment are also shown. d) A pair of L-MoSe₂ electrodes, on two opposite substrate layers, are assembled with cofferdam, electrolyte, and separator to fabricate an SC cell with a sandwich layout. e) The isolated cell is integrated into a highly integrated multilayered circuit substrate as an embedded component.

components. The achievement reported herein exhibits a critical step towards the practical application of micro-SCs in future highly integrated electronic systems.

2. Results and Discussions

2.1. Fabrication Route for 1T L-MoSe₂ Electrodes and SCs

The fabrication route for the 1T L-MoSe₂ nanosheets is given in **Figure 2**, and details can be found in the Experimental Section. First, the raw MoSe₂ powders (Figure S1, Supporting Information) were exfoliated through a modified liquid exfoliation method^[19] to obtain a mixture of few-layer 2H MoSe₂ nanosheets with a thickness of less than 5 nm and thicker ones (Figure S2, Supporting Information). The initial 2H-phase

MoSe₂ nanosheets demonstrated a perfect single-crystal structure (Figure 2a) and showed a typical trigonal prismatic atomic configuration of AB-type arrangement.^[21] A thin porous MoSe₂ film was fabricated on a Ti substrate using the electrostatic spray method, and the total electrode thickness was controlled at 215 nm (Figure S3, Supporting Information). Subsequently, a nanosecond laser beam with a wavelength of 355 nm was used to scan the electrode surface to trigger phase transformation of the MoSe₂ electrode from the 2H (Figure 2a) to 1T phase (Figure 2b). The unwanted areas can be ablated using the same laser at a much stronger power to render a high-resolution electrode array pattern. After laser treatment, the crystal structure of MoSe₂ changed from hexagonal to tetragonal symmetry, accompanied by an observable color change (Figure S4, Supporting Information).^[13,22] The concentration of defects in L-MoSe₂ increased dramatically, as indicated by the clear difference in their morphology

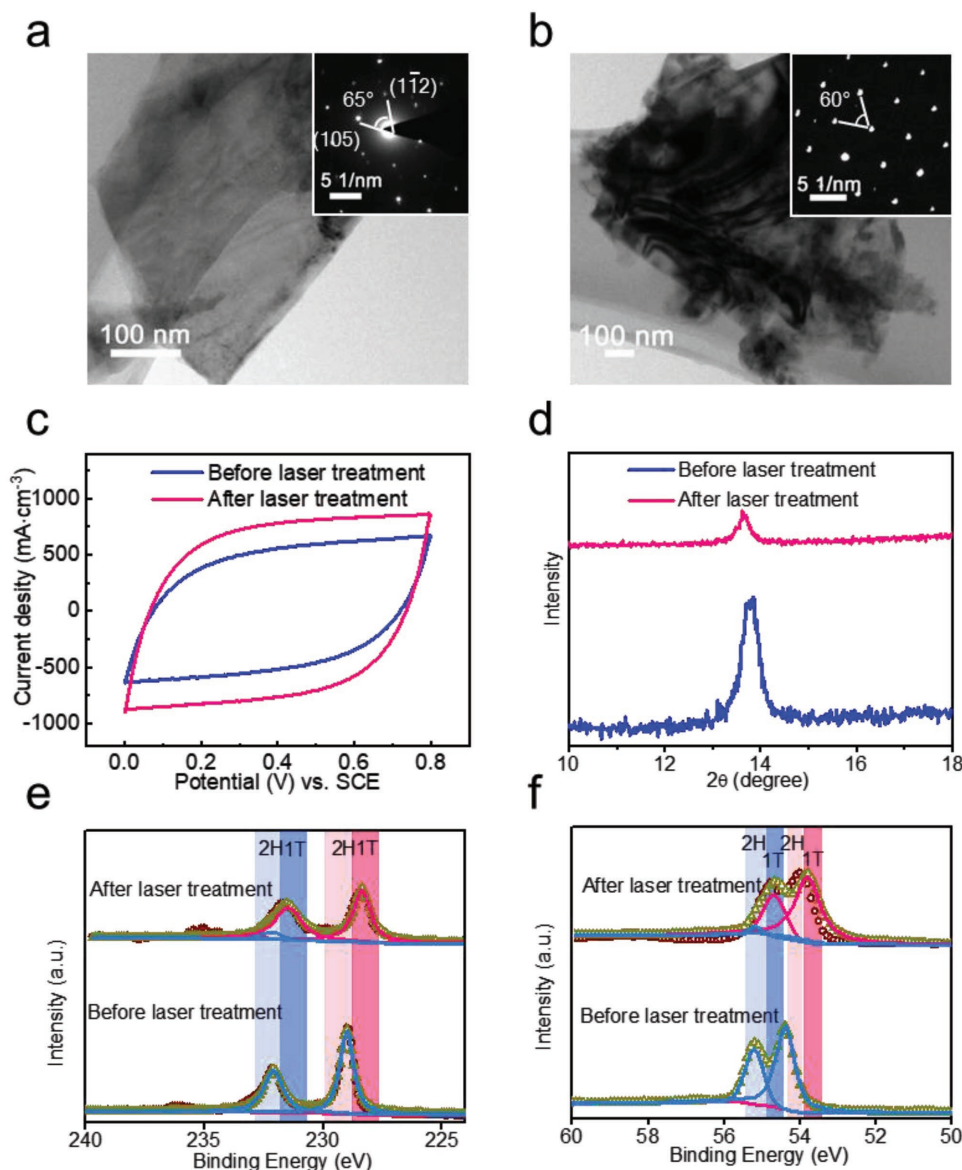


Figure 3. Characterization of the phase transition of 2H MoSe₂ nanosheets to 1T MoSe₂ nanosheets by laser irradiation. TEM images and selected area electron diffraction (SAED) patterns of a) a 2H phase MoSe₂ nanosheet and b) a 1T phase one. c) A comparison of CV curves of 2H (black) and 1T (red) MoSe₂ electrodes in Na₂SO₄ aqueous electrolyte at a scan rate of 10 V s⁻¹. d) A comparison of XRD pattern of 2H and 1T MoSe₂ nanosheets. High-resolution XPS spectra of e) Mo 3d and f) Se 3d in 2H and 1T MoSe₂ nanosheets.

(Figure 3a,b), and selected area electron diffraction (SAED) further confirmed the successful transformation of the 2H-phase MoSe₂ nanosheets. The 1T-phase product typically has an AbC-type octahedral atomic arrangement (Figure 2b), which is different with the 2H phase.^[23] Images of the 3D atomic arrangement of different phases of MoSe₂ are shown in Figure 2a,b. And more characterization related to the phase transformation will be discussed in the structural characterization part.

To fabricate the embedded SC components, a piece of prepreg (a half-cured thermally crosslinkable epoxy resin sheet, thickness: 76 μm) was sculpted by high-power laser to obtain an in-plane structure complementary to the patterned electrodes. This prepreg was used as both a binder and cofferdam to construct isolated cell units and to prevent leakage of electrolyte

(Figure 2c; Figure S5, Supporting Information). Subsequently, an SC was fabricated using the above obtained electrodes, cofferdam, electrolyte, and separator by a hot-lamination packaging technique with aligned position, which can be integrated as an embedded component in a highly integrated system (Figure 2d). Moreover, the packaging technique of the isolated cells is fully compatible with the industrial large-scale fabrication process of packaging substrates.

2.2. Structural Characterization of the MoSe₂ Nanosheets

Figure 3c demonstrates the cyclic voltammetry (CV) results of the L-MoSe₂ electrodes before and after laser treatment with

different laser powers to induce phase transformation. A laser power of 1.000 W (corresponding to a power intensity of $2.55 \times 10^6 \text{ W cm}^{-2}$) was chosen as the standard processing parameter, and a capacitance increase of around 50% can be obtained after laser treatment. The capacitance increase after laser treatment comes from the phase transformation. The capacitance of the electrode at high-frequency range mainly comes from the electric double layers, which is decided by the specific surface area, pore size distribution, and conductivity. After laser treatment, semiconducting 2H phase nanosheets are transformed into metallic 1T phase ones, which can facilitate the free electron tunnelling through the interface between the current collector and active material.

Next, X-ray diffraction (XRD, Figure 3d) and X-ray photoelectron spectroscopy (XPS, Figure 3e,f) were used to monitor the exfoliation and phase engineering processes. Compared to the XRD pattern of MoSe₂ powder (Figure S6, Supporting Information), the electrostatically sprayed film composed of MoSe₂ nanosheets showed a broader (002) peak and enhanced intensity of the (106) peak, which indicates that MoSe₂ nanosheets were randomly distributed by the electrostatic spray technique. Additionally, zeta potential measurements indicated that these MoSe₂ nanosheets were weakly negatively charged ($\approx -20 \text{ mV}$, Table S1, Supporting Information). Here, we adopted a laser beam to transform MoSe₂ nanosheets from 2H phase to 1T one. The 1T phase MoSe₂ has a reported bandgap energy of 0.64 eV, which is 0.81 eV lower than that of its 2H counterpart (1.45 eV), thus showing a much higher electrical conductivity.^[21] The effectiveness of phase engineering through laser irradiation can be confirmed by the XRD patterns, as shown in Figure 3d and Figure S7 in the Supporting Information. After laser irradiation treatment, the intensity of the (002) peak was weakened and its position shifted, indicating transformation to the 1T phase.^[13,24] Furthermore, XPS was used to measure the chemical states of the Mo and Se atoms in L-MoSe₂, as shown in Figure 3e,f and Figure S8 in the Supporting Information. The Mo 3d spectra of the L-MoSe₂ nanosheets display strong double peaks at 228.3 eV ($3d_{5/2}$) and 231.4 eV ($3d_{3/2}$), which indicates the formation of 1T-phase MoSe₂.^[18] Similarly, the spectra of Se 3d display two large peaks at 53.8 and 54.7 eV, which can also be attributed to 1T-phase MoSe₂.^[25] The yield of 1T-phase MoSe₂ nanosheets was almost 100%, which was a higher conversion rate than that of previously reported TMD electrodes.^[13] Notably, this laser-induced phase transformation is also feasible for MoTe₂ nanosheets, showing general applicability for TMD phase modulations (Figure S9, Supporting Information). Therefore, the laser-induced phase transformation is verified by the combined characterization techniques, including transmission electron microscopy (TEM), XRD, XPS, and Raman spectra (Figures 2,3; Figures S7–S9, Supporting Information). As for the mechanism for such phase transformation, a possible reason is the formation of Se or Te vacancies during laser irradiation process.^[20]

2.3. Electrochemical Performance Evaluation

The electrochemical performance of the fully packaged L-MoSe₂ SCs with a symmetric sandwich structure was performed

at scan rates ranging from 0.002 V s^{-1} to $10\,000 \text{ V s}^{-1}$ in an ionic liquid ($[\text{C}_2\text{MIm}]\text{BF}_4$) electrolyte (Figure 4a,b; Figure S10, Supporting Information). Ionic liquid electrolyte instead of aqueous one was selected to avoid any instability issues, such as oxidation and electro-oxidation of the electrode materials during cycling. The L-MoSe₂ SCs showed a high energy of 26.4 mWh cm^{-3} due to the high specific volumetric capacitance (26.1 F cm^{-3}) and operating voltage (2.7 V). More importantly, they exhibited an exceptionally enhanced rate performance with a near-rectangular CV curve (Figure 4a), even at an ultra-high scan rate of $10\,000 \text{ V s}^{-1}$ (Figure 4b), indicative of typical electric-double-layer behavior.^[26] This phenomenon is quite different from previous reports on semiconductive 2H MoSe₂ nanosheets prepared by hydrothermal method, which showed only moderate rate capability.^[27,28] When the devices work at high scan rates, the electric double layer behavior dominates in the energy storage process, indicated by the excellent rectangular shape. On the other hand, SCs based on recently reported carbon materials, in an attempt to attain high-rate performance, show a significantly decreased capacitance when the scan rate is above 200 V s^{-1} .^[8–10] In comparison, a linear dependence (Figure 4c) of the discharge current on the scan rate can be recognized up to at least 2000 V s^{-1} for our L-MoSe₂ SC (Figure 4d), which features a superior rate capacitance and power density, i.e., 1664 W cm^{-3} . Remarkably, such rate performance is much better than that of ever-reported SCs and commercial ones.^[10,29,30] The GCD curves (Figure 4e) showed a slightly distorted symmetric triangular shape, which can result from the self-discharge of SCs in the ionic liquid electrolyte and still indicate superior capacitive behavior.^[31] To evaluate the electrochemical performance of an SC with even higher mass loading, the thickness of the electrode was increased from 215 to 860 nm. The results show that the SC can maintain 82% of the specific capacitance even after this fourfold increase in the electrode mass loading (Figure 4f). Furthermore, our device performance showed no degradation after a hot-lamination process at the temperature of $120 \text{ }^\circ\text{C}$, which indicated that our embedded device was compatible with future low-temperature bonding/joining procedure for surface mountable components using low-sintering-temperature paste (such as commercial silver nanoparticle paste, typically sintered at less than $120 \text{ }^\circ\text{C}$). We also demonstrated that this laser treatment process can be used to convert 2H-phase MoTe₂ into 1T'-phase one, which also showed significantly improved electrochemical properties (Figure S11, Supporting Information). Therefore, this technology represents a universal strategy for phase engineering the TMD-based electrodes.

The superior electrochemical performance can be partially attributed to the intrinsically excellent electrical conductivity of the 1T MoSe₂ electrode in the $[\text{C}_2\text{MIm}]\text{BF}_4$ electrolyte. The equivalent series resistance (ESR) of L-MoSe₂ SCs is very small as shown in Figure 5a (3.2 and $8.4 \text{ } \Omega$ before and after cycling, respectively), which is even much smaller than that of reported carbon-based SCs.^[26,32] Also, the relaxation time constant τ_0 is very short, as shown in Figure 5b ($\tau_0 = 1/f_0$, 0.032 and 0.036 ms before and after cycling, respectively). Both of the small ESR and short τ_0 indicate the excellent ion and electron conductivity of L-MoSe₂ SCs. The oscillating curve in the middle-frequency range in Figure 5b can be related to the change in the ionic

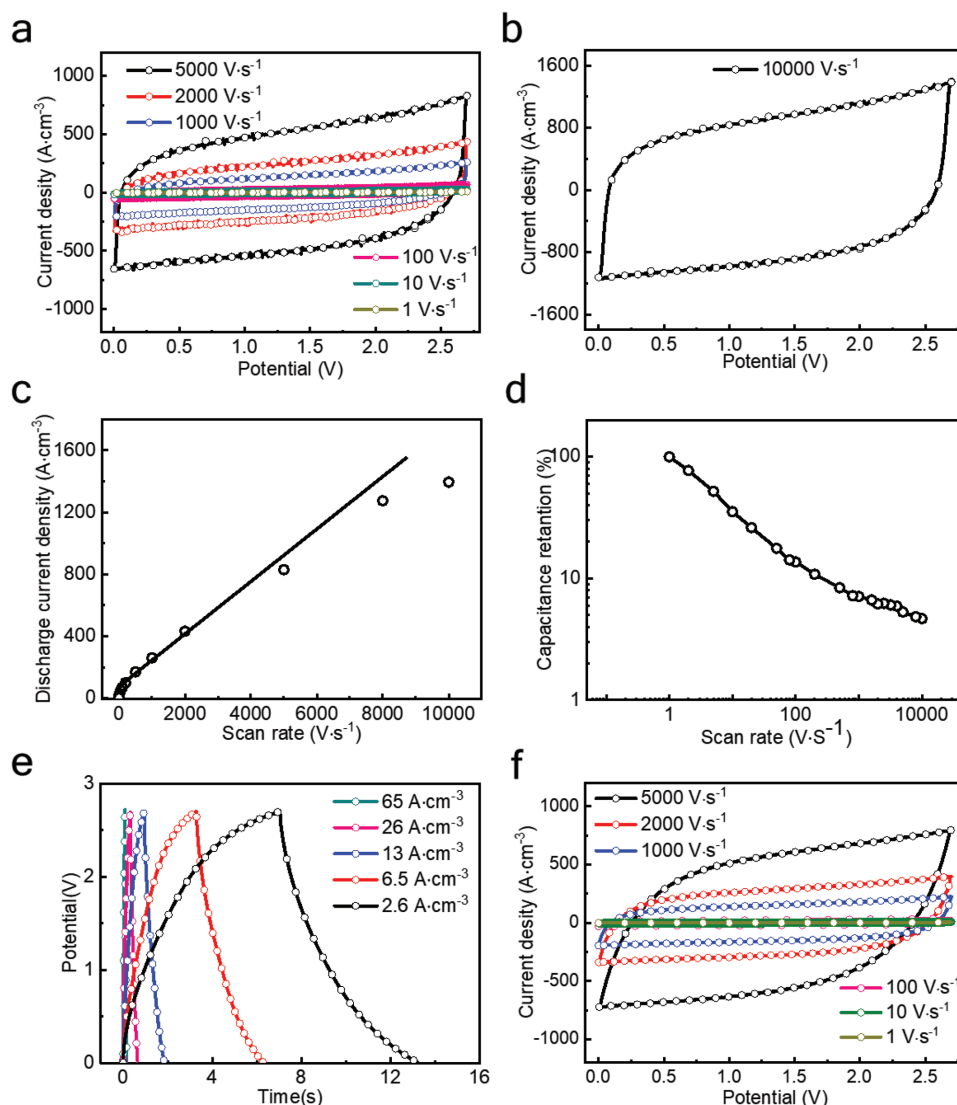


Figure 4. Characterization of the electrochemical properties (CV, GCD) of L-MoSe₂ nanosheet-based SC in [C₂MIm]BF₄ electrolyte. a,b) CV curves obtained at scan rates ranging from 1 V s⁻¹ to 10 000 V s⁻¹, demonstrating an excellent rate capability at ultrahigh scan rates. c) A plot of the discharge current as a function of scan rate, displaying a linear dependence up to 5000 V s⁻¹, suggesting ultrahigh power handling capability. d) Capacitance retention under high scan rates where the capacitance at 1 V s⁻¹ was treated as the initial value. e) GCD curves from 2.6 to 65 A cm⁻³. f) CV curves of L-MoSe₂ sandwich SCs with the electrode thickness of 860 nm in [C₂MIm]BF₄ electrolyte.

environment of the electrolyte.^[33] Such high frequency response could be the synergistic result of the excellent electron and ion transfer ability. The excellent electrical conductivity of the MoSe₂ electrode with ≈100% 1T phase ensures excellent electron transfer during cycling.^[13] The electrode prepared by electrostatic spray deposition is binder-free with randomly stacked MoSe₂ nanosheets, which could form abundant interstitial sites to facilitate free access of the electrolyte to the electrode surface, and thus contributes to the excellent ion-transport efficiency.^[6,34]

The stable ESR and τ_0 can also contribute to the superior stability of L-MoSe₂ SCs. A capacitance retention of 121.4% (Figure 5c) was observed after 1 000 000 cycles at 10 V s⁻¹, indicating the super-long cycle stability of our SC, which is beneficial for practical electronic applications. Such excellent

cycling stability at high frequency could be the synergistic result of the following factors: (1) The component packaging condition (in a glove-box) greatly reduced the content of oxygen and water, and the inert atmosphere inhibited side reactions at the interface between the electrode and electrolyte.^[35] (2) 1T phase nanosheets are intrinsically stable in our measurement since a good stability was reported when the temperature is less than 300 °C.^[20] Therefore, we can expect an excellent stability for our devices. As for the slightly increase in capacitance, one possible reason is that an improved wetting of the electrolyte on the nanosheets electrodes could be achieved after long-time immersing.^[36] Another factor influencing the capacitance is the morphology change after cycling. XRD, SEM, and TEM analyses of the MoSe₂ sample after long-term cycling were carried out (Figure 5d,e; Figure S12, Supporting Information). We found

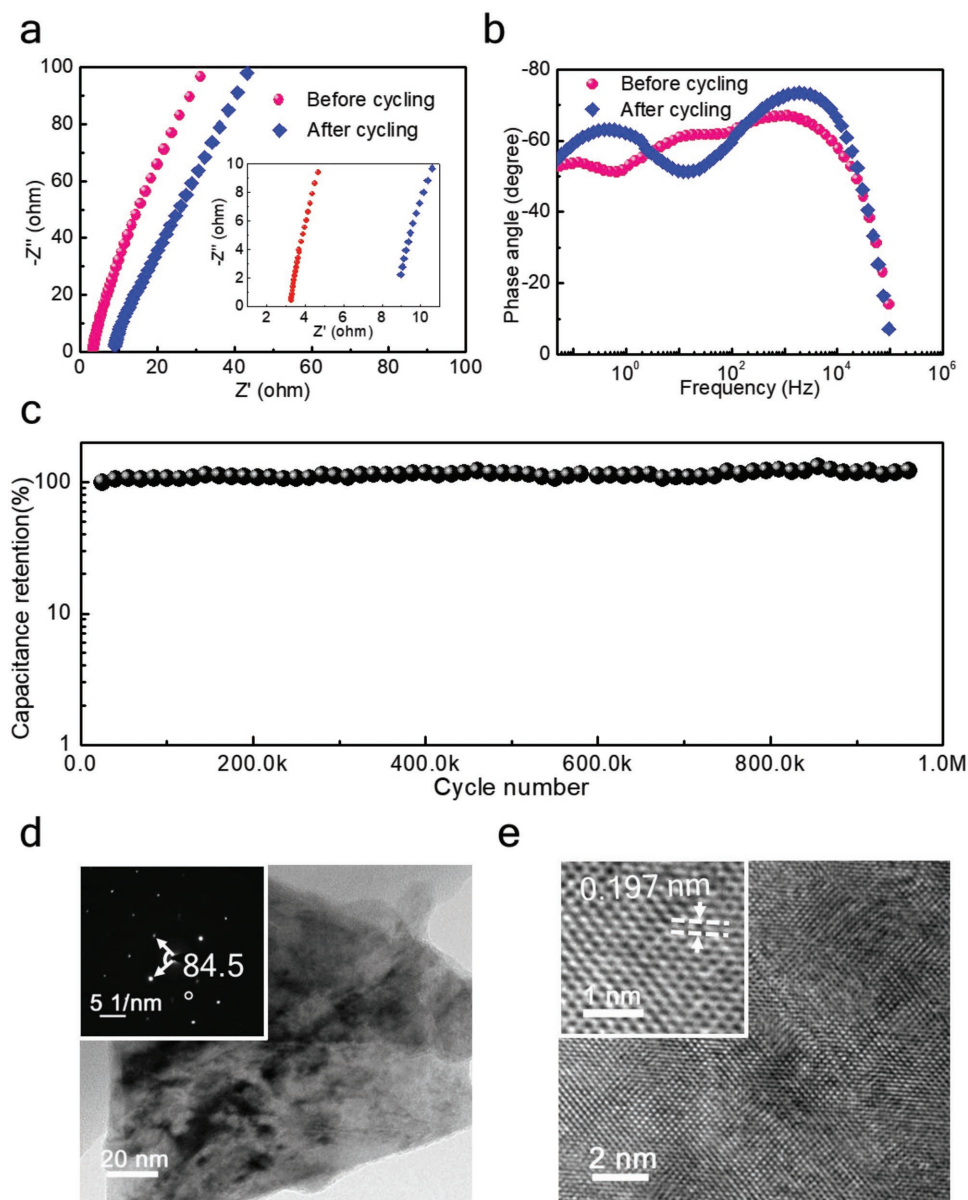


Figure 5. Characterization of the electrochemical properties (EIS, cycle stability) of L-MoSe₂ nanosheet-based SC in [C₂MIm]BF₄ electrolyte. a) Complex plane plots of the impedance before and after cycling, showing small values and an insignificant change in the ESR. b) Impedance phase angle versus frequency before and after cycling. The -45° phase angle occurred at $\approx 31\,640$ Hz and $\approx 27\,540$ Hz before and after 1 000 000 cycles. c) Cycling performance at a scan rate of 10 V s^{-1} , achieving a super-long-term cycling stability up to 1 000 000 cycles. d) TEM image of cycled MoSe₂ product with a flake shape, and inserted SAED result demonstrating a diffraction pattern contained an interfacial angle of about 84.5° . e) HRTEM image of the cycled MoSe₂ product in inset (d), showing an atomic arrangement of Ab type with a 0.197 nm interplanar spacing.

that a layer of porous nanoparticles was formed after cycling (Figure S12a,b, Supporting Information), and consequently the (002) peak in XRD pattern shifted with a tiny angle (-0.1° , Figure S12c, Supporting Information). We also found that a small portion (less than 5%) of the MoSe₂ nanosheets turned into polycrystalline with high defect density and distorted shape (Figure S12d–g and Table S2, Supporting Information).

For achieving a high specific energy density of the device, a higher working voltage is preferred. But it is quite a challenging task since high voltage can cause side reactions at the interface of the electrode and electrolyte. Here we further increased the

operating voltage to 3.5 V in the same ionic liquid electrolyte. As shown in Figure S13 (Supporting Information), the energy density and power density of the fully packaged SC component increased to 62.6 mWh cm^{-3} and 2113 W cm^{-3} , respectively. At such a high working voltage, a capacitance retention of 40% was observed after 3 000 000 cycles at 10 V s^{-1} .

To investigate the electrochemical performance of the L-MoSe₂ nanosheet-based SCs in more detail, a Ragone plot was constructed (Figure 6). Several state-of-the-art miniaturized energy storage devices, including commercial lithium thin-film batteries ($4\text{ V}/500\text{ }\mu\text{Ah}$),^[29] commercial surface-mount-device

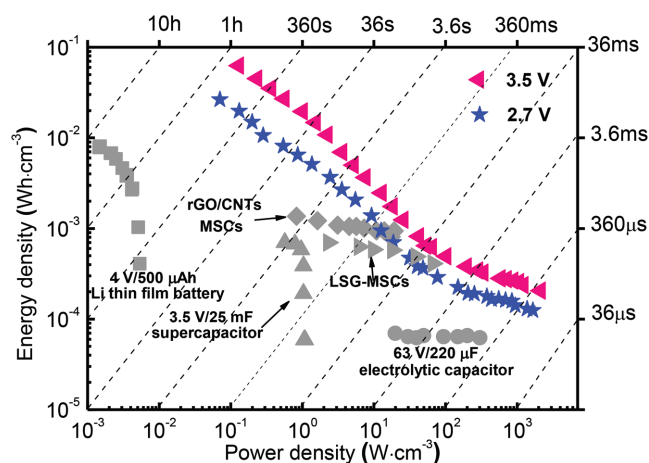


Figure 6. Performance evaluation and demonstration of embedded SCs based on 1T L-MoSe₂ electrodes. A Ragone plot of embedded SCs based on MoSe₂ nanosheets. Comparison of the energy and power density of embedded SCs with commercial lithium thin-film batteries, conventional SCs, AECs, and recently reported LSG-SCs and rGO/CNTs SCs.

(SMD) SCs (3.5 V/25 mF),^[30] commercial AECs (63 V/220 μF),^[9] laser-scribed graphene (LSG) SCs,^[37] and reduced graphene oxide (rGO)/carbon nanotube (CNT) SCs,^[38] are also shown in this plot. Compared with the carbon-based SCs, our L-MoSe₂-based ones demonstrate much higher energy densities under high charging/discharging rates. Remarkably, our embedded SCs can deliver a maximal volumetric energy density of 62.6 mWh cm⁻³, which is approximately one order of magnitude higher than that of the carbon-based SCs (10⁻⁴–10⁻³ Wh cm⁻³) and comparable to that of the lithium thin-film batteries (10⁻³–10⁻² Wh cm⁻³). Additionally, our SCs can manifest an ultrahigh power density of 2113 W cm⁻³, which is approximately three to four orders of magnitude higher than that of conventional SCs (0.1–1 W cm⁻³) and approximately ten times higher than that of the carbon-based SCs (1–100 W cm⁻³). Furthermore, this value is even higher than that of the commercial AECs (1–500 W cm⁻³), showing far superior rate performance at high frequency than the state-of-the-art carbon-based SCs (Table S3, Supporting Information). Moreover, due to the highly reliable electrode preparation and device fabrication processes, this embedded SC technology holds great promise for highly integrated miniaturized energy storage/management applications.

Currently commercially available AECs are large in size and in the form of isolated components, which occupy a large geometric surface area on top of a printed circuit board (PCB). For instance, commercially available personal computers use six isolated AEC units in the driver circuits for their central proceeding units (CPUs), which can filter the current and protect the CPU from damage by abrupt changes in the external voltage, even though they are much larger in size than most other components in such an integrated system. Comparatively, our embedded L-MoSe₂ SCs, featuring superior high-frequency filtering ability, high power density, and compact size, have the potential to cater to such applications and many others (as shown in Figure 1). As shown in Figure S14 (Supporting Information), our SC can be embedded into an integrated circuit

package substrate to light a red light-emitting diode (LED) for a few seconds, showing excellent energy storage ability. The SC technology developed here has significant advantages over conventional AECs, including the component size (one order of magnitude smaller), discharge rate performance (one order of magnitude higher), and flexibility in system design. All these features are essential for applications on the platforms of SiP and SoC technologies. Additionally, the fabrication techniques for our embedded SC are highly compatible with industrial large-scale processes, which may provide new solutions for energy management and high-frequency filtering in future high-integration systems.

3. Conclusion

In summary, we developed a universal method for modulating the phase characteristics of TMD electrode materials in an industry-adaptive manner. MoSe₂ nanosheets serve as a model material for the integration of novel 2D nanomaterials into embeddable high-performance SC components. The ultrahigh rate performance (up to 10⁴ Hz with a phase angle >60° and relaxation time of ≈32 μs) and superior cycle stability (insignificant capacitance loss even after 10⁶ cycles) of the embeddable SC components are far superior to those of commercial AECs and state-of-the-art SCs. The superior capacitive property and excellent energy density (62.6 mWh cm⁻³) can be ascribed to the excellent structural stability of the few-layer L-MoSe₂, the proper pore size distribution and the excellent electrical conductivity of the 1T metallic-phase electrode, which substantially improves electron and ion transportation. This work shows that TMD materials can be used for energy storage at rates exceeding 10 000 V s⁻¹, and even higher rates can likely be achieved after further optimization of the material composition and architecture. Furthermore, the fabrication method for the embedded SCs is highly compatible with industry-scale mass production, affording new and exciting opportunities in SiP and SoC applications.

4. Experimental Section

Preparation of 2H MoSe₂ Nanosheets: MoSe₂ nanosheets were prepared by a modified liquid exfoliation method.^[19] The MoSe₂ powder was purchased from Alpha Ltd. (Chengdu, China) and had an average diameter of ≈10 μm, as shown in Figure S1 in the Supporting Information. Typically, the MoSe₂ powder (0.3 g) was added in a mixed solvent of water (10 mL) and ethanol (20 mL), and the mixture was sonicated in a sonication bath (Xinzhij-Y92-IIDN) for 4 h at 0 °C. Then, the resultant dispersion was centrifuged at 5000 rpm for 10 min and the supernatant (top four-fifths of the centrifuged dispersion) was collected by pipette for use.

Preparation of the 1T-Phase L-MoSe₂ Nanosheet-Based Electrodes: A solution of MoSe₂ nanosheets in water–ethanol mixed solvent (3.22 mg mL⁻¹) was used to prepare MoSe₂ films on a Ti substrate by the electrostatic spray technique. The precursor was electrospayed under an operating voltage of 13 kV onto the surface of the substrate at an injection speed of 0.5 mm min⁻¹, and the temperature of the spray deposition process was kept at 50 °C for fast solvent evaporation to obtain a uniform MoSe₂ film. The thickness of the MoSe₂ film can be well controlled by this process. Then, the MoSe₂ film was exposed

to a laser beam (wavelength: 355 nm, model: Han's Laser EP-15-DW, nanosecond frequency, scanning line speed 4 m s^{-1}), and the typical processing parameter was scanning for one cycle with a working power of 1.000 W.

Characterization of Materials: The morphology and microstructure were characterized by field emission scanning electron microscopy (FE-SEM, HITACH S4800, Japan, working voltage of 5 kV) and TEM (FEI-G2 Spirit, Germany, working voltage of 300 kV). XPS (ESCALAB 250 Xi, Thermo Scientific, USA) measurements were performed to analyse the surface species and their chemical states. Deconvolution and spectral line fitting were carried out using the XPS Peak 4.0 software. Phase and crystallinity analyses were conducted by XRD (Bruker DS RINT2000/PC, Germany) using Cu K α radiation with $\lambda = 1.5418 \text{ \AA}$ (at diffraction angles ranging from 10° to 60° and a scan rate of 5° min^{-1}).

Characterization of SCs: The prototype SCs were evaluated by CV, GCD, and electrochemical impedance spectroscopy (EIS) using two electrochemical stations (VMP3-Bio-Logic, France, and CHI 660E, China). Only the single electrode was investigated by a three-electrode configuration in Na_2SO_4 (0.50 M) aqueous electrolyte, in which a Pt electrode and saturated calomel electrode (SCE) were used as the counter and reference electrodes, respectively. Other characterization for SCs, including EIS test and cycling stability, were done in an ionic liquid electrolyte. The EIS test was conducted in the frequency range between 100 kHz and 0.01 Hz with an amplitude of 5 mV at the open-circuit potential. The calculation details of the electrochemical performance of the SCs are shown in Section S1 in the Supporting Information.

Supporting Information

Supporting Information is available online from the Wiley Online Library or from the author.

Acknowledgements

Z.J., Y.W., and S.Y. contributed equally to this work. The authors thank the Local Innovative and Research Teams Project of Guangdong Pearl River Talents Program (2017BT01N111), Shenzhen Geim Graphene Center, the National Nature Science Foundation of China (Project Nos. 51578310 & 51607102), Guangdong Province Science and Technology Department (Project Nos. 2017A030313279 & 2015B010127009 & 2015A030306010), and Shenzhen Government (Project Nos. JCYJ20170412171720306 & JCYJ20150518162144944) for financial supports. C.Y., Y.W., S.Y. and Z.J. conceived and designed the study; Z.J., S.Y. and Y.W. performed the experiments; N.W., W.L., X.W. and L.S. provided helpful suggestions for analysis and manuscript revision; all authors discussed the results; C.Y., Z.J. and Y.W. wrote the manuscript, with contributions and feedback from all the authors. C.Y. supervised the research and discussed the results.

Conflict of Interest

The authors declare no conflict of interest.

Keywords

embeddable supercapacitors, high-frequency response, laser-induced phase transformation, MoSe_2 nanosheets, ultralong cycling stability

Received: October 8, 2018
Revised: November 25, 2018
Published online:

- [1] B. Xie, Y. Wang, W. Lai, W. Lin, Z. Lin, Z. Zhang, P. Zou, Y. Xu, S. Zhou, C. Yang, F. Kang, C.-P. Wong, *Nano Energy* **2016**, *26*, 276.
- [2] J. Lu, K.-S. Moon, J. Xu, C. P. Wong, *J. Mater. Chem.* **2006**, *16*, 1543.
- [3] ResearchInChina, *Global and China Aluminum Electrolytic Capacitor Market Report, 2013–2016*, <http://www.researchinchina.com/Htmls/Report/2014/6877.html> (accessed: June 2014).
- [4] M. Létiche, K. Brousse, A. Demortière, P. Huang, B. Daffos, S. Pinaud, M. Respaud, B. Chaudret, P. Roussel, L. Buchailot, P. L. Taberna, P. Simon, C. Lethien, *Adv. Funct. Mater.* **2017**, *27*, 1606813.
- [5] Y. Wang, W. Lai, N. Wang, Z. Jiang, X. Wang, P. Zou, Z. Lin, H. J. Fan, F. Kang, C.-P. Wong, C. Yang, *Energy Environ. Sci.* **2017**, *10*, 941.
- [6] J. Zhao, Y. Jiang, H. Fan, M. Liu, O. Zhuo, X. Wang, Q. Wu, L. Yang, Y. Ma, Z. Hu, *Adv. Mater.* **2017**, *29*, 1604569.
- [7] Z. S. Wu, Y. Zheng, S. Zheng, S. Wang, C. Sun, K. Parvez, T. Ikeda, X. Bao, K. Mullen, X. Feng, *Adv. Mater.* **2017**, *29*, 1602960.
- [8] W.-W. Liu, Y.-Q. Feng, X.-B. Yan, J.-T. Chen, Q.-J. Xue, *Adv. Funct. Mater.* **2013**, *23*, 4111.
- [9] D. Pech, M. Brunet, H. Durou, P. Huang, V. Mochalin, Y. Gogotsi, P.-L. Taberna, P. Simon, *Nat. Nanotechnol.* **2010**, *5*, 651.
- [10] C. Li, X. Zhang, K. Wang, X. Sun, G. Liu, J. Li, H. Tian, J. Li, Y. Ma, *Adv. Mater.* **2017**, *29*, 1604690.
- [11] M. R. Lukatskaya, S. Kota, Z. Lin, M.-Q. Zhao, N. Shpigel, M. D. Levi, J. Halim, P.-L. Taberna, M. W. Barsoum, P. Simon, Y. Gogotsi, *Nat. Energy* **2017**, *2*, 17105.
- [12] J. Feng, X. Sun, C. Wu, L. Peng, C. Lin, S. Hu, J. Yang, Y. Xie, *J. Am. Chem. Soc.* **2011**, *133*, 17832.
- [13] M. Acerce, D. Voiry, M. Chhowalla, *Nat. Nanotechnol.* **2015**, *10*, 313.
- [14] N. Choudhary, C. Li, H. S. Chung, J. Moore, J. Thomas, Y. Jung, *ACS Nano* **2016**, *10*, 10726.
- [15] K.-J. Huang, J.-Z. Zhang, Y. Fan, *Mater. Lett.* **2015**, *152*, 244.
- [16] H.-S. Kim, J. B. Cook, H. Lin, J. S. Ko, S. H. Tolbert, V. Ozolins, B. Dunn, *Nat. Mater.* **2017**, *16*, 454.
- [17] R. Kappera, D. Voiry, S. E. Yalcin, B. Branch, G. Gupta, A. D. Mohite, M. Chhowalla, *Nat. Mater.* **2014**, *13*, 1128.
- [18] Y. Qu, H. Medina, S.-W. Wang, Y.-C. Wang, C.-W. Chen, T.-Y. Su, A. Manikandan, K. Wang, Y.-C. Shih, J.-W. Chang, H.-C. Kuo, C.-Y. Lee, S.-Y. Lu, G. Shen, Z. M. Wang, Y.-L. Chueh, *Adv. Mater.* **2016**, *28*, 9831.
- [19] J. N. Coleman, M. Lotya, A. O'Neill, S. D. Bergin, P. J. King, U. Khan, K. Young, A. Gaucher, S. De, R. J. Smith, I. V. Shvets, S. K. Arora, G. Stanton, H.-Y. Kim, K. Lee, G. T. Kim, G. S. Duesberg, T. Hallam, J. J. Boland, J. J. Wang, J. F. Donegan, J. C. Grunlan, G. Moriarty, A. Shmeliov, R. J. Nicholls, J. M. Perkins, E. M. Grieveson, K. Theuvsissen, D. W. McComb, P. D. Nellist, V. Nicolosi, *Science* **2011**, *331*, 568.
- [20] S. Cho, S. Kim, J. H. Kim, J. Zhao, J. Seok, D. H. Keum, J. Baik, D.-H. Choe, K. J. Chang, K. Suenaga, S. W. Kim, Y. H. Lee, H. Yang, *Science* **2015**, *349*, 625.
- [21] U. Gupta, B. S. Naidu, U. Maitra, A. Singh, S. N. Shirodkar, U. V. Waghmare, C. N. R. Rao, *APL Mater.* **2014**, *2*, 092802.
- [22] D. Voiry, A. Mohite, M. Chhowalla, *Chem. Soc. Rev.* **2015**, *44*, 2702.
- [23] D. Voiry, H. Yamaguchi, J. Li, R. Silva, D. C. B. Alves, T. Fujita, M. Chen, T. Asefa, V. B. Shenoy, G. Eda, M. Chhowalla, *Nat. Mater.* **2013**, *12*, 850.
- [24] K. Leng, Z. Chen, X. Zhao, W. Tang, B. Tian, C. T. Nai, W. Zhou, K. P. Loh, *ACS Nano* **2016**, *10*, 9208.
- [25] Y. Liu, M. Zhu, D. Chen, *J. Mater. Chem. A* **2015**, *3*, 11857.
- [26] Z. S. Wu, K. Parvez, X. Feng, K. Müllen, *Nat. Commun.* **2013**, *4*, 2487.
- [27] K.-J. Huang, J.-Z. Zhang, J.-L. Cai, *Electrochim. Acta* **2015**, *180*, 770.
- [28] S. K. Balasingam, J. S. Lee, Y. Jun, *Dalton Trans.* **2015**, *44*, 15491.
- [29] J. Zhu, A. S. Childress, M. Karakaya, S. Dandeliya, A. Srivastava, Y. Lin, A. M. Rao, R. Podila, *Adv. Mater.* **2016**, *28*, 7185.

- [30] Y. Shao, M. F. El-Kady, C. W. Lin, G. Zhu, K. L. Marsh, J. Y. Hwang, Q. Zhang, Y. Li, H. Wang, R. B. Kaner, *Adv. Mater.* **2016**, *28*, 6719.
- [31] d. S. Firmiano, E. Geraldo, A. C. Rabelo, C. J. Dalmaschio, A. N. Pinheiro, E. C. Pereira, W. H. Schreiner, E. R. Leite, *Adv. Energy Mater.* **2014**, *4*, 1301380.
- [32] W. Gao, N. Singh, L. Song, Z. Liu, A. L. M. Reddy, L. Ci, R. Vajtai, Q. Zhang, B. Wei, P. M. Ajayan, *Nat. Nanotechnol.* **2011**, *6*, 496.
- [33] D. Kuang, S. Ito, B. Wenger, C. Klein, J.-E. Moser, R. Humphry-Baker, S. M. Zakeeruddin, M. Gratzel, *J. Am. Chem. Soc.* **2006**, *128*, 4146.
- [34] X. Yang, C. Cheng, Y. Wang, L. Qiu, D. Li, *Science* **2013**, *341*, 534.
- [35] T. Brousse, P.-L. Taberna, O. Crosnier, R. Dugas, P. Guillemet, Y. Scudeller, Y. Zhou, F. Favier, D. Bélanger, P. Simon, *J. Power Sources* **2007**, *173*, 633.
- [36] H. Peng, J. Zhou, K. Sun, G. Ma, Z. Zhang, E. Feng, Z. Lei, *ACS Sustainable Chem. Eng.* **2017**, *5*, 5951.
- [37] M. F. El-Kady, V. Strong, S. Dubin, R. B. Kaner, *Science* **2012**, *335*, 1326.
- [38] M. Beidaghi, C. Wang, *Adv. Funct. Mater.* **2012**, *22*, 4501.